EXTENDED PDF FORMAT
SPONSORED BY
usb®
www.usbweb.com

Experimental Observation of Nonlinear Traveling Waves in Turbulent Pipe Flow

Björn Hof, *et al.*

Science **305**, 1594 (2004);
DOI: 10.1126/science.1100393

The following resources related to this article are available online at www.sciencemag.org (this information is current as of August 30, 2008):

Updated information and services, including high-resolution figures, can be found in the online version of this article at:
http://www.sciencemag.org/cgi/content/full/305/5690/1594

Supporting Online Material can be found at:
http://www.sciencemag.org/cgi/content/full/305/5690/1594/DC1

A list of selected additional articles on the Science Web sites **related to this article** can be found at:

http://www.sciencemag.org/cgi/content/full/305/5690/1594#related-content

This article has been **cited by** 71 article(s) on the ISI Web of Science.

This article appears in the following **subject collections**:
Physics, Applied
http://www.sciencemag.org/cgi/collection/app_physics

Information about obtaining **reprints** of this article or about obtaining **permission to reproduce this article** in whole or in part can be found at:
http://www.sciencemag.org/about/permissions.dtl

Science (print ISSN 0036-8075; online ISSN 1095-9203) is published weekly, except the last week in December, by the American Association for the Advancement of Science, 1200 New York Avenue NW, Washington, DC 20005. Copyright 2004 by the American Association for the Advancement of Science; all rights reserved. The title *Science* is a registered trademark of AAAS.

Biological Relevance of This Mechanism

Conductance of uncharged NH_3, versus NH_4^+ ion, can solve several biological problems. First, because K^+ channels conduct the very similarly sized NH_4^+ ion, there is the reverse possibility that an NH_4^+ ion channel could "leak" potassium and hence leak membrane potential in eukaryotes. Amt/MEP proteins are not permeable to any other ions (*26*). Transport of only uncharged NH_3 and not NH_4^+ assures this selectivity against all ions that would require replacement for their hydration shell while in the narrow portion of the channel. The energetic cost of removing even a single water of hydration from an ion is prohibitive. Second, NH_4^+ or any other ion is progressively energetically unstable as it approaches the center of the hydrophobic bilayer, whereas NH3 is much less so because it is electrically neutral. Potassium channels for example, have solved the problem by providing 16 carbonyl oxygens, 8 around each K^+ ion position on the way into the channel (*34*). Each oxygen offers a partial charge of 0.4 electrons to stabilize each K^+ ion. The KcsA channel also provides a water-filled cavity in the most energetically costly position at the center of the bilayer (*35*). The narrow hydrophobic channel of AmtB solves this energetic problem, as it also selects against the ionic form of NH_4^+ or any organic molecule larger in cross section than a single NH_3. Third, passage of uncharged NH_3 versus NH_4^+ would not leak proton motive force in conduction. Thus, neither energy nor any counter ion would be needed to accumulate ammonia.

Note added in proof: In a recent publication (*37*), it is shown that Am conductance by RhBG in oocytes is electroneutral, in contrast to the currents reported by the same group for another homolog (*26*), and can explain observations of electric currents in oocytes by an indirect mechanism. If general to the Amt/MEP/Rh family (Fig. 1), this would eliminate the only data that we discuss as potentially inconsistent with the mechanism we deduce.

References and Notes

1. J. Broach *et al.*, *J. Bacteriol.* **128**, 86 (1976).
2. M. A. Knepper *et al.*, *Physiol. Rev.* **69**, 179 (1989).
3. M. H. Saier Jr. *et al.*, *Biochim. Biophys. Acta* **1422**, 1 (1999).
4. G. H. Thomas *et al.*, *Mol. Microbiol.* **37**, 331 (2000).
5. A. M. Marini *et al.*, *EMBO J.* **13**, 3456 (1994).
6. A. M. Marini *et al.*, *Mol. Cell. Biol.* **17**, 4282 (1997).
7. D. Blakey *et al.*, *Biochem. J.* **364**, 527 (2002).
8. S. L. Hackette *et al.*, *J. Biol. Chem.* **245**, 4241 (1970).
9. R. Tate *et al.*, *Mol. Plant Microbe Interact.* **11**, 188 (1998).
10. M. R. Atkinson, A. J. Ninfa, *Mol. Microbiol.* **29**, 431 (1998).
11. G. Coutts *et al.*, *EMBO J.* **21**, 536 (2002).
12. A. Javelle *et al.*, *J. Biol. Chem.* **279**, 8530 (2004).
13. A. M. Marini *et al.*, *Trends Biochem. Sci.* **22**, 460 (1997).
14. E. Soupene *et al.*, *J. Bacteriol.* **184**, 3396 (2002).
15. H. Nielsen *et al.*, *Protein Eng.* **10**, 1 (1997).
16. J. H. Park, M. H. Saier Jr. *J. Membr. Biol.* **153**, 171 (1996).
17. Z. S. Derewenda *et al.*, *J. Mol. Biol.* **252**, 248 (1995).
18. A. Roos, W. F. Boron, *Physiol. Rev.* **61**, 296 (1981).
19. N. A. Priver *et al.*, *Biochemistry* **32**, 2459 (1993).
20. D. Fu *et al.*, *Science* **290**, 481 (2000).
21. S. Khademi *et al.*, unpublished data.
22. E. Soupene *et al.*, *Proc. Natl. Acad. Sci. U.S.A.* **95**, 7030 (1998).
23. E. Soupene *et al.*, *Proc. Natl. Acad. Sci. U.S.A.* **99**, 3926 (2002).
24. M. Y. Wang *et al.*, *Plant Physiol.* **103**, 1259 (1993).
25. J. Meier-Wagner *et al.*, *Microbiology* **147**, 135 (2001).
26. U. Ludewig *et al.*, *J. Biol. Chem.* **277**, 13548 (2002).
27. C. M. Westhoff *et al.*, *J. Biol. Chem.* **277**, 12499 (2002).
28. C. M. Westhoff *et al.*, *J. Biol. Chem.* **279**, 17443 (2004).
29. R. M. Siewe *et al.*, *J. Biol. Chem.* **271**, 5398 (1996).
30. C. Sohlenkamp *et al.*, *Plant Physiol.* **130**, 1788 (2002).
31. A. M. Marini *et al.*, *Nature Genet.* **26**, 341 (2000).
32. E. Soupene *et al.*, *Proc. Natl. Acad. Sci. U.S.A.* **99**, 7769 (2002).
33. E. Soupene *et al.*, *Proc. Natl. Acad. Sci. U.S.A.* **101**, 7787 (2004).
34. J. H. Morais-Cabral *et al.*, *Nature* **414**, 37 (2001).
35. Y. Jiang *et al.*, *Nature* **417**, 523 (2002).
36. Materials and methods are available as supporting material on *Science* Online.
37. U. Ludewig, *J. Physiol. (London)*, in press; published online 29 July 2004 (10.1113/jphysiol.2004.067728).
38. We thank J. Finer-Moore for her enlightened counsel, J. Holten for his assistance at the Advanced Light Source (ALS) beamline 8.3.1, and M. Mann for assistance in molecular biology. E. Soupene and S. Kustu suggested structure determination of an AmtB, and we thank them for providing an *Aquifex amtB* clone pJES1331, a solubilized cell pellet, and partially purified *Aquifex* protein. Supported by NIH grant no. GM24485 (R.M.S.). Coordinates (accession codes: apo, 1U77; Am, 1U7G; and MA, 1U7C) and structure factors (accession codes: apo, RCSB023331; Am, RCSB023340; and MA, RCSB023336) of the structures have been deposited in the Research Collaboratory for Structural Bioinformatics Protein Data Bank.

Supporting Online Material
www.sciencemag.org/cgi/content/full/305/5690/1587/DC1
Materials and Methods
References and Notes

24 June 2004; accepted 5 August 2004

REPORTS

Experimental Observation of Nonlinear Traveling Waves in Turbulent Pipe Flow

Björn Hof,[1]*† Casimir W. H. van Doorne,[1]* Jerry Westerweel,[1] Frans T. M. Nieuwstadt,[1] Holger Faisst,[2] Bruno Eckhardt,[2] Hakan Wedin,[3] Richard R. Kerswell,[3] Fabian Waleffe[4]

Transition to turbulence in pipe flow is one of the most fundamental and longest- standing problems in fluid dynamics. Stability theory suggests that the flow remains laminar for all flow rates, but in practice pipe flow becomes turbulent even at moderate speeds. This transition drastically affects the transport efficiency of mass, momentum, and heat. On the basis of the recent discovery of unstable traveling waves in computational studies of the Navier-Stokes equations and ideas from dynamical systems theory, a model for the transition process has been suggested. We report experimental observation of these traveling waves in pipe flow, confirming the proposed transition scenario and suggesting that the dynamics associated with these unstable states may indeed capture the nature of fluid turbulence.

Turbulence is one of the most common examples of complex and disordered dynamical behavior in nature. Typically, the motion of clouds, weather patterns, river flows, and even the flow from a faucet are turbulent. Yet the way in which turbulence arises and sustains itself is not understood even in laboratory experiments with well-controlled boundary conditions. The first study of this kind was undertaken by Reynolds (*1*) in 1883. He investigated the transition to turbulence in pipe flow and his observations have posed a riddle ever since. Whereas stability theory predicts that pipe flow will remain laminar for all flow rates (*2*), in practice pipe flow becomes turbulent even at moderate speeds. In contrast to other laminar-turbulence transitions, where primary and secondary instabilities of the laminar flow provide guidance, the transition process in pipe flow has remained a near total mystery. In pipes, turbulence sets in suddenly and fully, with no intermediate states and without a clear stability boundary.

Pipe flow can be described by a single dimensionless parameter, the Reynolds number $Re = UD/\nu$, where U is the mean (or bulk) flow speed, D the pipe diameter, and ν the kinematic viscosity of the fluid. In the laminar state, the flow profile is parabolic and the flow rate is proportional to the pressure gradient. This picture changes markedly when the flow rate is increased and turbulent flow commences. The ensuing flow is temporally and spatially highly disordered and viscous drag and dissipation are strongly increased. In typical pipe flows, turbulence sets in spontaneously at Reynolds numbers as low as 2000; however, in carefully designed experiments the transition point can be delayed to Reynolds numbers as large as 100,000 (*3*). On the basis of the recent discovery of traveling wave and periodic solutions to the governing Navier-Stokes equation (*4–10*), a new transition scenario for pipe and related shear flows has been suggested (*11–13*). All of the observed solutions are believed to be unstable and cannot persist individually in practical flows because of the inevitable presence of ambient noise. Yet as the Reynolds number is increased, more and more of these unstable solutions are believed to arise. In their multitude they can support long-lived disordered flows in which the flow state transiently visits these unstable solutions before returning to the laminar state. In mathematical terms, the unstable states form a chaotic repellor in phase space (*11*), which gives rise to long-lived turbulent transients. As the Reynolds number is increased further, this chaotic repellor is believed to evolve into a turbulent attractor, i.e., an attracting region in phase space, dynamically governed by the large number of unstable solutions, which sustains disordered turbulent flow indefinitely. The laminar state is still stable, but it is reduced from a global to a local attractor. As the Reynolds number increases, the basin of the turbulent attractor grows, whereas that of the laminar state diminishes (i.e., the number of initial conditions that lead to turbulent flow markedly increases). Consequently, smaller and smaller perturbations to the laminar flow are sufficient to cause a transition to turbulence. Some consensus between theoretical ideas and actual experimental observations has been found in that the stability boundary, and hence the basin of attraction of the laminar state, indeed decreases in proportion to $1/Re$ (*14*). However, direct evidence that unstable traveling waves are relevant for turbulent flows in practice is missing.

For the dynamics of flow patterns in shear flows, Waleffe (*8*, *9*, *15–17*) has proposed a self-sustaining process. Vortices with a streamwise orientation move fast fluid from the center toward the wall and simultaneously lift slow fluid from the walls to the center, creating local anomalies in the streamwise velocity called streaks. These streaks become inflexionally unstable. Nonlinear self-interaction of the unstable modes regenerates the streamwise vortices closing the feedback loop, thus sustaining these flow states against viscous decay. The traveling waves reflect this process. Hence, the most important structural features of these traveling waves are the streamwise vortices and streaks. The wavy nature of these states can most readily be identified in the periodic modulation of the low-speed streaks. The waves travel in the streamwise direction at a phase speed typically slightly larger than the bulk velocity (*4*, *5*). Because all of the numerically observed traveling waves are (most likely) unstable, they cannot persist in practical pipe flows but may be observable as transients, if indeed they are relevant to the turbulent flow. The aim of this study is to identify these traveling waves in experimental turbulent pipe flow.

A schematic of the experimental set-up is shown in Fig. 1 (supporting online material text) (*18*, *19*). For the present measurements, fully developed laminar pipe flow [i.e., for which the velocity profile was parabolic (fig. S3)] was destabilized 350 pipe diameters from the inlet by means of injecting an impulsive jet for 1.5 s ($\sim 1.9D/U$) through a hole of 1-mm diameter in the pipe wall. The jet was injected orthogonally to the main flow with a volume flux of approximately 50% of the flux in the pipe. The so-created turbulent flow region was inspected 150 pipe diameters downstream of the injection point with a 500-Hz high-speed stereoscopic particle image velocimetry system. As found in our own studies and in agreement with previous observations (*20*, *21*), a distance of $150D$ is more than sufficient to allow all transients inflicted by the perturbation mechanism to subside. Hence, the observations presented here can be regarded as typical flow structures representative for turbulent pipe flow at the particular Reynolds number. For visualization purposes, the water was seeded with 10-μm tracer particles that were neutrally buoyant, and a radial cross-sectional plane of the pipe was illuminated by a frequency-doubled pulsed neodymium-doped yttrium lithium fluoride laser. This plane was viewed by two cameras positioned in forward scatter on opposite sides of the light sheet at 45° to the observation plane (figs. S1 and S2). The full three-component velocity field at about 2600 points in the observation plane was reconstructed from the displacement of the tracer particles between subsequent images recorded by the cameras (*22*). The passage of turbulent structures was recorded in a series of 1000 contiguous measurements at sampling frequencies between 60 and 500 Hz. A high degree of precision (figs. S4 to S8) was achieved with the use of a test section that minimizes optical distortion and an optimized calibration procedure to align the stereoscopic camera set-up (fig. S2) (*19*).

Our first investigation is concerned with localized turbulent structures, called "puffs" (*21*), which occur at relatively low Reynolds numbers ($1800 < Re < 2500$). Puffs are isolated patches of turbulent flow, which are advected downstream at ~95% of the bulk velocity. Turbulent puffs typically extend 5 to ~20 pipe diameters, depending on the Reynolds number. The transition regions between the laminar flow and the turbulent flow at either end of the puff are referred to as the downstream and upstream edge, and these can be identified by the characteristic velocity change during the passage of a puff (*20*, *21*). A velocity field in a cross-sectional plane close to the upstream edge of a puff measured at $Re = 2000$ is shown in Fig. 2A. Here, the laminar flow profile is subtracted from the measured downstream velocity component. Regions of high velocity relative to the lam-

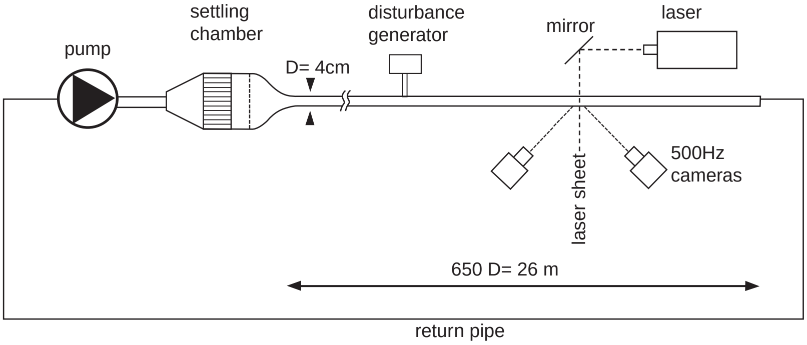

Fig. 1. Experimental apparatus: Water is pumped by way of a settling chamber into a 26-m-long straight pipe that has a diameter of $D = 4$ cm. The settling chamber as well as the inlet shape were designed to minimize disturbances from the inlet (*13*). The entire pipe is thermally insulated to avoid heat convection, which would distort the flow profile. The fully developed laminar flow is perturbed $350D$ from the inlet, and particle image velocimetry measurements are performed another $150D$ downstream.

---

[1]Laboratory of Aerodynamics and Hydrodynamics, Delft University of Technology, Leeghwaterstraat 21, 2628 CA Delft, Netherlands. [2]Fachbereich Physik, Philipps-Universität Marburg, 35032 Marburg, Germany. [3]Department of Mathematics, University of Bristol, Bristol, BS8 1TW, UK. [4]Departments of Mathematics and Engineering Physics, University of Wisconsin, Madison, WI 53706, USA.

*These authors contributed equally to this work.
†To whom correspondence should be addressed. E-mail: b.hof@wbmt.tudelft.nl

inar profile are shown in red, regions of low velocity relative to the laminar profile are shown in blue, and transverse components are indicated by arrows. Whereas the wall region contains six distinct high-speed streaks, the central region is occupied by a large low-speed streak extending three arms in the radial direction. This streak configuration is in notable agreement with a C_3 symmetric traveling wave (C_m specifies an *m*-fold rotational symmetry) found by Faisst and Eckhardt (*4*) (Fig. 2B). Generally, the flow is dominated by the streaks, and the spanwise motions are critical but much weaker. The cross-stream motions are therefore more quickly overwhelmed by fluctuations resulting from the inherent instabilities of the traveling waves. Although the experimentally observed state does not display a full periodic cycle in the streamwise direction, certain features of the state persist over a large portion of the turbulent puff. In particular, we observed that the high-speed streaks are considerably more static than the low-speed streaks, which was also observed numerically (*4*, *5*). To quantify the persistence of the symmetry features, we calculated an azimuthal correlation of the streamwise velocity component in the vicinity of the pipe wall. A correlation calculated from the measurements close to the upstream end of the puff is shown in Fig. 3A. Peaks at 60°, 120°, and 180° manifest the presence of six distinct high-speed streaks in the near-wall region. The correlation curve in Fig. 3B, measured close to the downstream (leading) edge of the puff, only has a peak at 120°. The flow pattern observed here consists of three high-speed streaks close to the wall spaced at 120° and a low-speed region in the central part of the pipe. Traveling wave modes with a C_3 symmetry containing three high-speed streaks in the near-wall region have also been calculated numerically (*5*). The resulting correlations measured along the entire puff are shown in Fig. 3C. Throughout the downstream end of the puff, a single correlation peak was found. At a distance of about 4*D*, the single peak bifurcates into three peaks (at about 60°, 120°, and 180°), which persist throughout the upstream part of the turbulent puff. Visual inspection of the velocity fields confirms that indeed three high-speed streaks are present throughout the downstream section of the puff and six

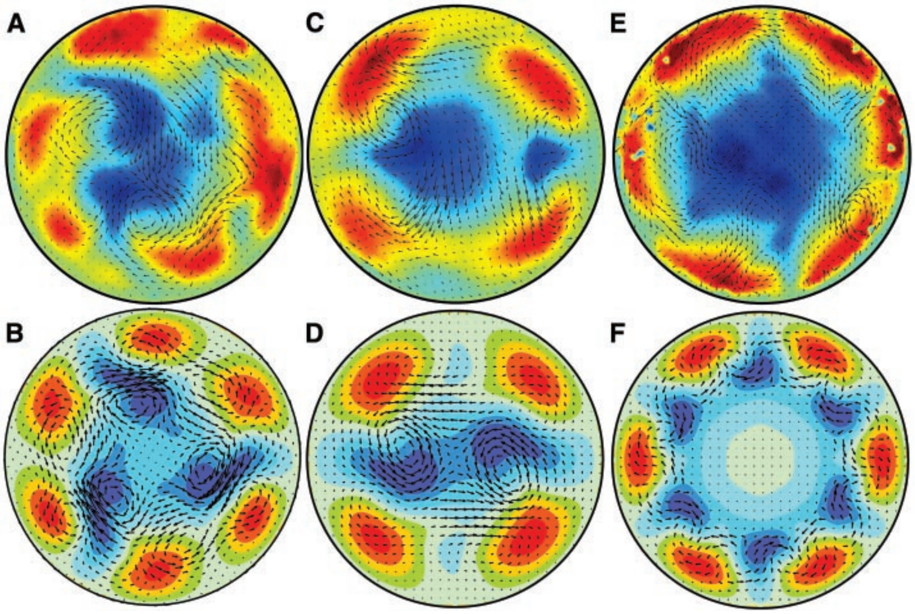

Fig. 2. Comparison of experimentally (top) and numerically (bottom) observed streak patterns. Velocity components in the plane are indicated by arrows, and the downstream component is indicated by color coding, where red or blue signifies velocities faster or slower than the parabolic profile, respectively. The color coding for the experimental flow patterns (top row) ranges from plus (dark red) to minus (dark blue) 0.6*U*; the numerical flows (bottom row) range from plus (dark red) to minus (dark blue) 0.4*U*. The maximum in-plane velocities are one order of magnitude smaller than the maximum out-of-plane components. (**A**) Experimentally observed state in turbulent puff at $Re = 2000$. (**B**) Cross-sectional slice through a C_3 symmetric streamwise traveling wave observed numerically at $Re = 1250$ (*4*, *5*). (**C**) C_2 symmetric state observed in a turbulent puff at $Re = 2500$. (**D**) Corresponding numerical C_2 traveling wave ($Re = 1360$). (**E**) C_6 symmetric state found in the experiment at $Re = 5300$ for fully turbulent flow. The streak configuration in the near-wall region resembles that of a numerical C_6 traveling wave (**F**) ($Re = 2900$). The dominance of the low-speed streak in the central part of (E) is more characteristic of a C_3 traveling wave, suggesting that (E) may result from nonlinear interactions of C_3 and C_6 traveling waves.

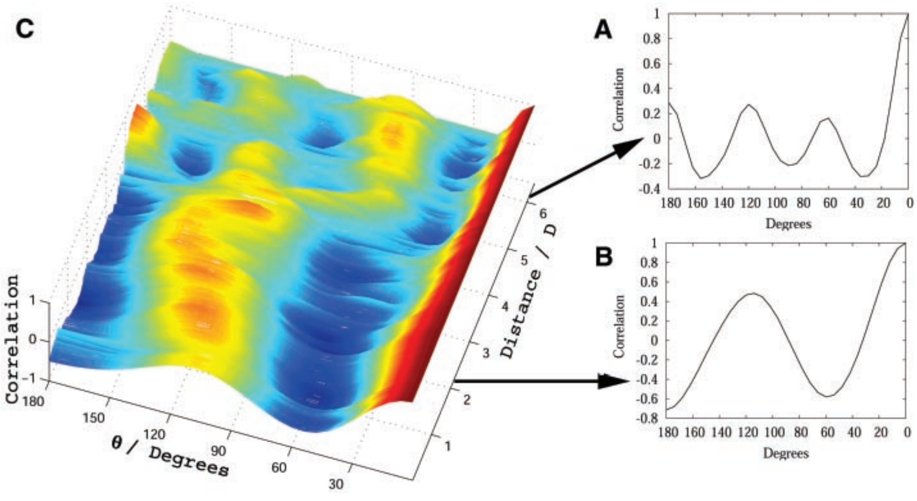

Fig. 3. (**A**) Azimuthal correlation close to the upstream edge of a puff ($Re = 2000$). (**B**) Azimuthal correlation close to the downstream edge of the puff. (**C**) Display of the azimuthal correlations from 500 consecutive measurements, taken while a turbulent puff traveled through the measurement plane. Distances are measured with respect to the first measurement, which was taken at the downstream end of the puff. The temporal spacing of the measurements was converted into a spatial one by multiplication with the advection speed (Taylor's hypothesis). This approximation is justified because the puff advection speed is more than an order of magnitude larger than the in-plane velocity components. Colors represent the amplitude of the correlation ranging from dark red (+1) for maximal correlation to dark blue (–1) for anticorrelated data. A single correlation peak is observed for distance <4, which then splits up into three peaks for distance >4, indicating a change in the streak pattern from three to six high-speed streaks in the near-wall region. Correlations were calculated according to $C(\phi,r)=\int_0^{2\pi} U(\phi,r)U(\phi+\theta,r)d\theta$ for five radii in the interval $0.9 \geq r/(D/2) \geq 0.7$, where *r* is the radial distance from the pipe centerline, and for each measurement plane the radius showing the maximum correlation (largest difference between the maxima and minima) was selected.

streaks are present for the remainder of the puff. Qualitatively, the same result has been found for all puffs investigated at this Reynolds number. This result is surprising, in that features of the turbulent puff—i.e., the number and spacing of high-speed streaks—appear to be determined by a small number of unstable states.

The C_2 traveling wave, shown in Fig. 2C, has been observed at *Re* = 2500. Again, the streak pattern is in excellent agreement with that of its numerical counterpart (Fig. 2D). The numerically calculated traveling waves in Figs. 2 and 4 are shown for lower Reynolds numbers than the experimentally observed traveling waves. As pointed out by Wedin and Kerswell (*5*), the change in the form of the numerical solutions for an increasing Reynolds number is very small, and the main features and symmetry properties remain unchanged. The flow state (Fig. 2E) was observed in a turbulent slug (*21*) at *Re* = 5300. The streak/vortex configuration in the near-wall region resembles a numerically observed C_6 traveling wave (Fig. 2F). Overall, the measured structure is more likely to be a combination of C_6 and C_3 modes (Fig. 2), which is in accord with the increased complexity of the observed structures at higher Reynolds numbers. In this Reynolds number regime, excellent agreement was found for statistical quantities such as the mean velocity and root mean square velocity fluctuations between the experimental measurements and numerical simulations of turbulent flow (figs. S6 to S8) (*19*, *23*, *24*). For plane Couette and channel flow, the exact traveling waves in the numerical model already capture turbulence statistics (*17*) remarkably well, which can be seen as an indication of the intrinsic role of the traveling wave states to the turbulent flow.

Finally, we observed a C_4 symmetric traveling wave at *Re* = 3000 (Fig. 4).This wave transient showed a periodic modulation similar to that of a C_4 symmetric wave over several periods and allowed us to estimate its wavelength (±SD) to (1.1 ± 0.15) *D*. The periodic modulation is most evident in the up and down motion of the left low-speed streak shown in Fig. 4A. The three figures show half of one periodic cycle. The corresponding C_4 traveling wave (Fig. 4B) has an optimal wavelength of 0.97*D*, which is in excellent agreement with the experimentally determined value. As in Fig. 2E, the central low-speed region of the experimental traveling wave is more pronounced than that of its numerical counterpart.

The experimental observation of unstable states can be rationalized by comparing the characteristic time scales. The experimental observation time is about 10*D/U* and the largest unstable Lyapunov exponent is about 0.07, implying a characteristic time scale for the decay of a traveling wave transient of about 14*D/U*. Thus, if the experimentally observed turbulent state is close to a three-dimensional traveling wave at one instance, the observation time is not long enough for it to evolve far away.

In conclusion, signatures of unstable traveling wave modes have been observed in surprising clarity and agreement with numerical studies (*4*, *5*). Spatial features of these wave states persist over large time intervals in turbulent pipe flow. These insights into the dynamics and symmetry of streaks open up further avenues for application of turbulent and chaos control (*25*, *26*) strategies.

These observations support a theoretical scenario in which the turbulent state is organized around a few dominant traveling waves. Although such a proposal is in line with dynamical systems ideas (*27*), there has been no experimental or theoretical evidence for its applicability to shear flow turbulence before the present study. The observation of the traveling wave states shows that concepts from dynamical systems theory can contribute greatly to our understanding of turbulence. Indeed, because unstable solutions have been calculated for a variety of shear flows (*4–10*), we speculate that these states play a universal role in shear flow turbulence.

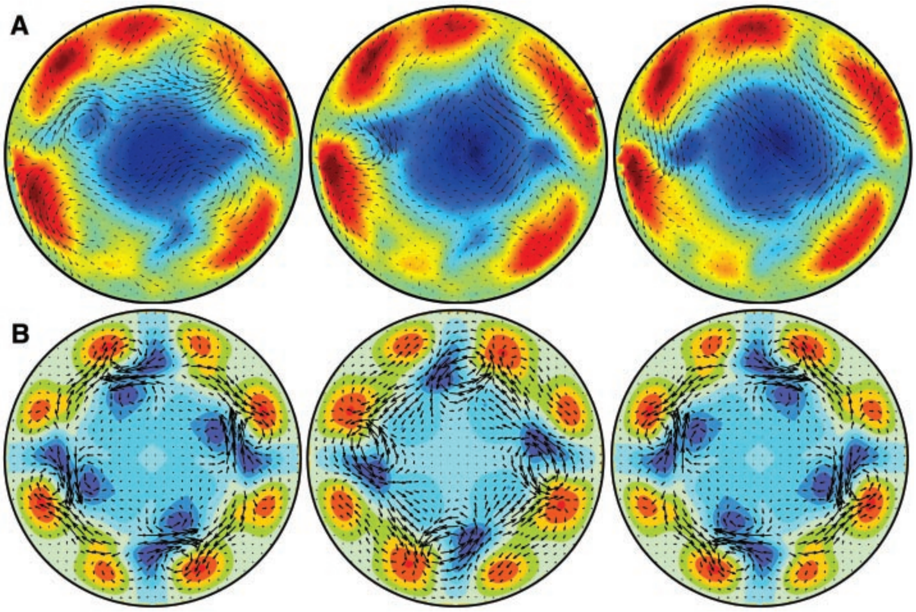

Fig. 4. Velocity scales and color coding are the same as for Fig. 2. (**A**) Half a wavelength of a C_4 traveling wave transient observed in fully turbulent flow at *Re* = 3000. The frames are spaced by λ/4 where the wavelength (±SD) was measured as λ = 1.1*D* ± 0.15. The low-speed streak on the left-hand side shows the clearest modulation. (**B**) Exact C_4 traveling wave (*Re* = 1650) as observed in the numerical simulations. Again, the frame spacing is λ/4 and the wavelength is λ = 0.97*D*. The strong low-speed streak at the center of the experimental traveling wave is not found in the numerical traveling wave and is more characteristic for a C_2 traveling wave. In analogy to the C_6 symmetric wave in Fig. 2E, this suggests that the experimental state may result from interactions of C_4 and the C_2 traveling waves.

References and Notes

1. O. Reynolds, *Proc. R. Soc. London* **35**, 84 (1883).
2. P. G. Drazin, W. H. Reid, *Hydrodynamic Stability* (Cambridge Univ. Press, Cambridge, 1981).
3. W. Pfenniger, in *Boundary Layer and Flow Control*, G. V. Lachman, Ed. (Pergamon, Oxford, 1961), pp. 970–980.
4. H. Faisst, B. Eckhardt, *Phys. Rev. Lett.* **91**, 224502 (2003).
5. H. Wedin, R. R. Kerswell, *J. Fluid Mech.* **508**, 333 (2004).
6. M. Nagata, *J. Fluid Mech.* **217**, 519 (1990).
7. R. M. Clever, F. H. Busse, *J. Fluid Mech.* **344**, 137 (1997).
8. F. Waleffe, *Phys. Rev. Lett.* **81**, 4140 (1998).
9. F. Waleffe, *J. Fluid Mech.* **435**, 93 (2001).
10. G. Kawahara, S. Kida, *J. Fluid Mech.* **449**, 291 (2001).
11. H. Faisst, B. Eckhardt, *J. Fluid Mech.* **504**, 343 (2004).
12. A. Schmiegel, B. Eckhardt, *Phys. Rev. Lett.* **79**, 5250 (1997).
13. B. Eckhardt, A. Mersmann, *Phys Rev. E* **60**, 509 (1999).
14. B. Hof, A. Juel, T. Mullin, *Phys. Rev. Lett.* **91**, 244502 (2003).
15. J. M. Hamilton, J. Kim, F. Waleffe, *J. Fluid Mech.* **287**, 317 (1995).
16. F. Waleffe, *Phys. Fluids* **9**, 883 (1997).
17. F. Waleffe, *Phys. of Fluids* **15**, 1517 (2003).
18. A. A. Draad, G. D. C. Kuiken, F. T. M. Nieuwstadt, *J. Fluid Mech.* **377**, 267 (1998).
19. C. W. H. van Doorne, thesis, Delft University of Technology (2004).
20. A. G. Darbyshire, T. Mullin, *J. Fluid Mech.* **289**, 83 (1995).
21. I. J. Wygnanski, F. H. Champagne, *J. Fluid Mech.* **59**, 281 (1973).
22. A. K. Prasad, *Exp. Fluids* **29**, 103 (2000).
23. J. G. M. Eggels *et al.*, *J. Fluid Mech.* **268**, 175 (1994).
24. C. W. H. van Doorne, J. Westerweel, F. T. M. Nieuwstadt, *Proceedings of the EUROPIV 2* (Springer-Verlag, Zaragoza, Spain, 2003).
25. T. Shinbrot, C. Grebogi, E. Ott, J. A. Yorke, *Nature* **363**, 411 (1993).
26. H. Choi, P. Moin, J. Kim, *J. Fluid Mech.* **262**, 75 (1994).
27. I. Procaccia, *Nature* **333**, 498 (1988).
28. Supported by the European Union network on stirring and mixing (B.H.), the Foundation of Fundamental Research on Matter (B.H., C.W.H.v.D., F.T.M.N., and J.W.), Deutsche

F.T.M.N., and J.W.), Deutsche Forschungsgemeinschaft (H.F. and B.E.), the Engineering and Physical Sciences Research Council (H.W. and R.R.K.) and the NSF (F.W.). Part of the experimental equipment was supplied by La Vision GmbH.

Supporting Online Material
www.sciencemag.org/cgi/content/full/305/5690/1594/DC1
Materials and Methods
Figs. S1 to S8
Tables S1 and S2
References

17 May 2004; accepted 30 July 2004

Mesophase Structure-Mechanical and Ionic Transport Correlations in Extended Amphiphilic Dendrons

B.-K. Cho,[1]* A. Jain,[1]* S. M. Gruner,[2] U. Wiesner[1]†

We have studied the self-assembly of amphiphilic dendrons extended with linear polyethylene oxide (PEO) chains and their ion complexes. Keeping the dendron core and linear PEO chain compatible allows for the combination of dendritic core-shell and conventional block copolymer characteristics for complex mesophase behavior. An unexpected sequence of crystalline lamellar, cubic micellar ($Pm\bar{3}n$), hexagonal columnar, continuous cubic ($Ia\bar{3}d$), and lamellar mesophases is observed. Multiple phase behavior within single compounds allows for the study of charge transport and mechanical property correlations as a function of structure. The results suggest an advanced molecular design concept for the next generation of nanostructured materials in applications involving charge transport.

The generation of supramolecular structures by self-assembly of molecular building blocks has become a powerful tool in designing enhanced material properties (*1*, *2*). Molecular engineering of the interface in microphase-separated domains is believed to be a key to the precise manipulation of supramolecular structures. To this end, a variety of molecular building blocks with rod (*3*), disk (*4*), and linear (*5*) type architecture have already been combined. Recently, dendrimers and their segments, dendrons, have fostered scientific interest as another class of building blocks. They are attractive because their particular shape introduces curved interfaces and because large numbers of functional groups can be readily introduced into a single molecule (*6*–*8*). Their unique structural features might lead to phase behavior that is quite different from that of conventional linear building blocks (*9*). Indeed, the dendrimer/dendron-periphery interface has been systematically controlled by either tethering different generations or periphery groups (*10*–*12*), and micellar structures with complicated lattices have been found in benzyl ether–based dendrons as a function of temperature (*13*, *14*). Despite theoretical predictions of a rich phase behavior (*15*), observed phases to date reveal only lamellar, columnar, or micellar packing. In particular, the existence of three-dimensional (3D) cubic network structures important for potential applications has not been demonstrated.

Here we report on third-generation amphiphilic dendrons extended by linear polyethylene oxide (PEO) chains synthesized as described in (*16*). Although several molecules with varying PEO molecular weights were studied, we will focus on two compounds, **1** and **2** (Fig. 1), which exhibit multiple phases that combine the behavior of linear block copolymers with that of dendritic systems. The mesophases were accessible through temperature changes and include crystalline lamellar (k_1, k_2), micellar (mc), hexagonal columnar (hex), continuous cubic (cc), lamellar (lam), and disordered (dis). Molecular masses of compounds **1** and **2** were determined to be 4600 and 7500 g/mol by matrix-assisted laser desorption ionization time-of-flight (MALDI-TOF) mass spectrometry. Based on these molecular masses and the density of each block, the hydrophilic volume fractions (f) were calculated to be 0.41 and 0.62 for **1** and **2**, respectively. Polydispersities (M_w/M_n) from MALDI-TOF mass spectrometry and gel permeation chromatography (GPC) were found to be less than 1.05. In contrast to most previous combinations of coil-dendron systems, the interface of these linearly extended dendrons is modeled in the middle of the dendritic structure rather than at the focal point (*17*–*20*). The hydrophilic part is composed of linear PEO plus a PEO-like dendritic core, whereas the hydrophobic fraction consists of eight docosyl peripheries (*21*, *22*). In this way, structural features of phase-separated dendritic core-shell architectures are combined with the ability to fine tune volume fractions through simple linear chain extension. Furthermore, linear and branched chain topologies are combined within one domain of the microphase-separated material.

Thermal behavior of compounds **1** and **2** was studied by differential scanning calorimetry (DSC) and transitions corroborated by dynamic mechanical spectroscopy (DMS) and temperature-dependent small-angle x-ray scattering (SAXS). The results are summarized in Table 1. DSC was run at a rate of 10°C/min, and transition temperatures were determined at peak maxima. Isochronal temperature step measurements at a frequency of 0.5 rad/s and shear amplitude in the linear regime (<2%) were performed on an advanced rheometrics expansion system (ARES) to identify the melting temperatures of the docosyl peripheries, order-order transitions (OOTs), and order-disorder transitions (ODTs). In DSC data, **1** and **2** show two

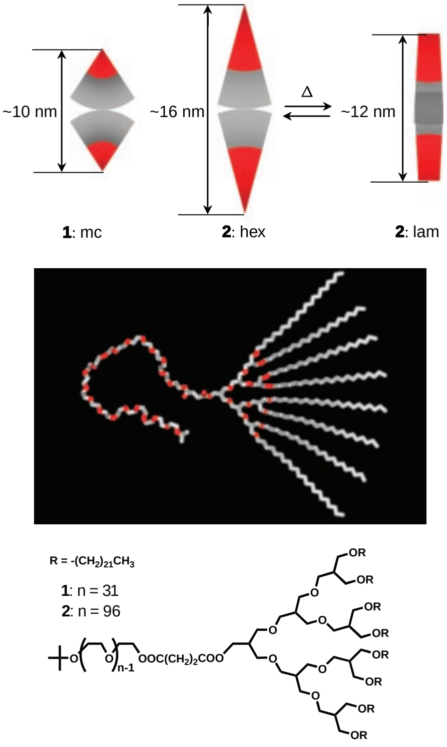

Fig. 1. Molecular architecture of extended amphiphilic dendrons **1** and **2**. Oxygen-containing segments are shown in red. (**Top**) Schematics of the type of molecular packing in different mesophases along with the respective dimensions consistent with SAXS data analyses and molecular models (red, hydrophilic parts; gray, hydrophobic parts). The schematics are meant to illustrate aspects of the local packing behavior only.

Department of Materials Science and Engineering and [2]Department of Physics, Cornell University, Ithaca NY 14853.
*These authors contributed equally to this work.
†To whom correspondence should be addressed. E-mail: ubw1@cornell.edu